The promotion effect of π-π interactions in Pd NPs catalysed selective hydrogenation

Miao Guo
Dalian Institute of Chemical Physics, Chinese Academy of Sciences
Sanjeevi Jayakumar
Dalian Institute of Chemical Physics
Xiangtao Kong
Anyang Normal University
Chunzhi Li
Dalian Institute of Chemical Physics
He Li
Dalian Institute of Chemical Physics https://orcid.org/0000-0003-0830-0844
Jian Chen
Zhejiang Normal University
Meng-Fei Luo
Qihua Yang (yangqh@dicp.ac.cn)
Dalian Institute of Chemical Physics https://orcid.org/0000-0002-1118-3397

Article

Keywords: catalysis, nanoparticles, covalent organic frameworks, non-covalent interactions

Posted Date: September 9th, 2021

DOI: https://doi.org/10.21203/rs.3.rs-871287/v1

Version of Record: A version of this preprint was published at Nature Communications on April 1st, 2022.
See the published version at https://doi.org/10.1038/s41467-022-29299-0.

Abstract

The utilization of weak interactions to improve the catalytic performance of supported metal catalysts is an important strategy for catalysts design, but still remains a big challenge. Herein, the weak interactions nearby the Pd nanoparticles (NPs) were finely tuned by using a series of imine-linked covalent organic frameworks (COFs) with different conjugation skeletons. The Pd NPs embedded in pyrene-COF were ca. 3 to 10-fold more active than those in COFs without pyrene in the hydrogenation of aromatic ketones/aldehydes, quinolines and nitrobenzene, though Pd have similar size and surface structure. With acetophenone (AP) hydrogenation as a model reaction, systematic studies imply that the π-π interaction of AP and pyrene rings in the vicinity of Pd NPs could significantly reduce the activation barrier in the rate-determining step. This work highlights the important role of non-covalent interactions beyond the active sites in modulating the catalytic performance of supported metal NPs.

Introduction

Inspired by biocatalysis, engineering the microenvironment of supported metal nanoparticles (NPs) to enhance their catalytic activity and selectivity has attracted a great amount of research interests[1-3]. The specific physicochemical microenvironment surrounding the metal NPs may significantly regulate their catalytic behaviour and is considered to be as important as the size, shape and metal-support interactions[4-6]. Hence, the fundamental understanding and the rational modulation of microenvironment nearby the metal NPs have become an important topic in the field of heterogeneous catalysis.

The assembly of organic ligands or polymers on metal surface is a general approach to construction a specific microenvironments in the vicinity of metal NPs[7-10]. The steric confinement effects created by the surface modifiers can effectively improve the selectivity via modulating the adsorption mode of the substrates[11-12], regulating the coordination of reactants on catalytic centers[13] and even manipulating the binding strength of intermediates[14-15]. For instance, the selectivity of C=O hydrogenation in cinnamaldehyde and furfural hydrogenation can be greatly increased via modulating the adsorption mode of the substrates on metal surface by construction of crowded “fence” on the Pt or Pd metal surface with the densely self-assembled monolayers (SAM) modifiers[11-12]. The organic modifiers can also interact with reactants or intermediates to be hydrogenated and thus affect the overall catalytic performance. For example, the surface modified chiral ligands can promote the enantioselectivity in metal NPs catalysed enantioselective hydrogenations via the weak interactions (e. g. H-bond, π-π no-covalent interactions) [16-17].

The nanospace of porous materials is another desirable platform to modulate the weak interactions surrounding the metal NPs through the specific functional groups integrated in the porous materials[18-20]. The functional groups of the porous material could regulate the interaction of the substrates[18-19] or the reaction intermediates[20], thereby to affect the activity and selectivity of the confined metal NPs. Recently, our group reported that the phosphine ligands in the vicinity of Ru NPs which preferentially interact with

COOH of benzoic acid can behave like a “regulator”, making inactive Ru NPs active in benzoic acid hydrogenation under mild conditions[19]. In most cases, the effect of microenvironment entangles with the alteration of the electronic and steric structure of metal NPs. Studies on using solely the weak interaction to modulate the catalytic performance of metal NPs have rarely been reported.

The principle challenging issue for utilization of weak interactions to regulate the catalytic performance of metal NPs is the lack of host materials with precisely designed organic moieties and pore structure at molecular level. Imine-linked covalent organic frameworks (COFs), featuring abundant conjugated aromatics, imine bonds and functional side chains, could be an ideal host material to engineering the weak interactions surrounding the metal NPs[21-24]. Although the promotion effect of COFs has been recently reported in organic transformations[25] or for immobilized metal complex in asymmetric catalysis[26], the comprehensive understanding of the substrate-COFs weak interactions and their effects on the catalyticperformance of metal NPs are still lacking.

In this work, the imine-linked COFs with different chemical composition and topologic structure were employed to modulate the weak interactions surrounding Pd NPs. With almost identical surface geometric and electronic structures, Pd NPs hosted in pyrene-containing COF (Py-COF) are more active than those in COFs without the pyrene moiety in the selective hydrogenation of polar functional groups (C=O, C=N, NO_2, C=C-O) of aromatic compounds. The systematic thermodynamic, kinetic studies and DFT calculations imply that the p-p interactions of the substrates and pyrene rings orderly arranged in pyrene-COF can direct the preferential adsorption of carbonyl group on Pd surface and reduce the activation barrier in the rate determining step to enhance the activity.

Results And Discussion

Synthesis and characterizations of Pd NPs confined in imine-linked COFs

A new and stable pyrene-containing COF (Py-COF) was synthesized by condensation of 1, 3, 6, 8-tetrakis (4-aminophenyl) pyrene (Py) and 2, 5-dimethoxyterephthalaldehyde (DMTA) (**Figure 1a**). The characteristic C=N vibration at 1612 cm^{-1} in the Fourier transform infrared spectroscopy (FT-IR) spectrum (**Figure S1a**) and chemical shifts at 157 ppm assigned to C=N in the solid-state ^{13}C CP-TOSS NMR spectrum (**Figure 1b**) indicate the successful formation of Py-COF with the imine linkage. The diffraction peaks at 3.8°, 5.8°, 7.6° and 23.4° in the PXRD pattern of Py-COF (**Figure 1c**) can be assigned to the (110), (210), (300) and (001) facets, respectively. The simulated PXRD patterns of the eclipsed AA stacking conducted by Materials Studio Software are in good agreement with the experimental PXRD patterns with a C2/m space group (**Figure S1b**). The Pawley refinement cell parameters are a = 36.927 Å, b = 31.363 Å, c = 4.047 Å, α = 92°, β = 110° and γ = 89°, with good agreement factors R_{wp} = 6.96% and R_p = 8.96% for Py-COF. Py-COF has a microporous structure with a BET surface area of 1183 $m^2 g^{-1}$ and pore volume of 1.3 $cm^3 g^{-1}$ (**Figure 1d**). The pore size of Py-COF is mainly distributed at about 1.6 nm, which agrees well with the theoretical data (1.7 nm) calculated by the AA stacking model.

The above result indicates that Py-COF has a well-stacked structure. Furthermore, almost identical PXRD patterns to the fresh sample were obtained after treatment of Py-COF in hot water, concentrated HCl and 14 M NaOH (**Figure 1e**), suggesting the high chemical and structural stability of Py-COF.

Other imine-linked COFs (Be-COF, TB-COF) with different topological structure and composition were synthesized according to the literature methods (**Figures 1a, S2**)[27-28]. The formation of imine-linked COFs was confirmed by FT-IR characterization (**Figure S3a**). The powder X-ray diffraction (PXRD) patterns show that Be-COF and TB-COF have high crystallinity with eclipsed AA stacking mode (**Figure S3b**), consistent with the reported results.[27,28] The Be-COF has BET surface area of 2076 $m^2 g^{-1}$, pore volume of 1.3 $cm^3 g^{-1}$ and pore size of 2.8 nm and TB-COF has BET surface area of 1234 $m^2 g^{-1}$, pore volume of 0.73 $cm^3 g^{-1}$ and pore size of 2.8 nm (**Figures S3c, S3d**). Be-COF and TB-COF both have higher BET surface area and larger pore size than those of Py-COF.

Py-COF, Be-COF and TB-COF with different conjugated skeleton were chosen as models to investigate the influence of non-covalent interactions on the catalytic performance of Pd NPs considering their different tendency to form p-p interaction with aromatic compounds[29]. The three COFs with the imine-linkage could be ideal supports for hosting ultrafine metal NPs due to the strong coordinating ability of imine with metal ions[30]. Pd NPs were loaded in COFs by the traditional wet impregnation-reduction method. High-resolution transmission electron microscopy (HR-TEM) and TEM images show that Pd NPs embedded in the three COFs have particle size of ~1.7 nm (**Figure S4).** The high-angle annular dark field scanning transmission electron microscopy (HAADF-STEM) images confirm the HR-TEM results (**Figures 2a, 2c, S5a**). The energy dispersive X-ray spectroscopy (EDS) results of the representative Pd/Py-COF show that the Pd NPs are in close contact with N and C, implying the existence of organic moieties in the vicinity of Pd NPs (**Figure 2b**). It should be noted that the ultrafine Pd NPs of 1.7 nm on Py-COF could still be obtained with 10 wt% Pd (**Figure S4b**), implying the unique characters of COFs in stabilizing ultra-fine metal NPs even at high metal loading amounts. The XRD patterns of Pd/COFs are similar to those of the parent COFs and no diffraction peaks assigned to Pd NPs could be observed, implying the well retained crystalline structure after Pd loading and the absence of large Pd particles (**Figure S6**). The Pd dispersion measured by CO adsorption is respectively 26.2%, 26.1% and 24.2 for Pd/Py-COF, Pd/Be-COF and Pd/TB-COF (**Table S1**), showing that all the Pd/COFs have similar Pd surface area.

In situ FT-IR spectra of CO adsorption was first conducted to characterize the surface properties of Pd NPs confined in the COFs. As shown in **Figures 2d and S5b**, Pd/Py-COF, Pd/Be-COF and Pd/TB-COF show the linear-bonded CO at ~2045 cm^{-1} together with the bridge-bonded CO at ~1915 cm^{-1}. It should be mentioned that the linear to bridge ratio (L/B ratio) for the three catalysts is almost the same (**Table S1**), suggesting that Pd NPs in the three COFs may have similar electronic and surface geometric structure. The identical Pd 3d binding energies (BEs) and Pd^0/Pd^{2+} ratio obtained by X-ray photoelectron spectroscopy (XPS) characterization further confirm that Pd NPs in the three COFs have similar surface electronic structure and reduction degree (**Figures 2e, S5c, Table S1**). In comparison with Pd/C, the Pd 3d BEs of Pd/COFs show a red shift of 0.1 eV, possibly related with the electron donation from imine to Pd

NPs. The electronic structure of Pd NPs was further investigated using the CO stripping voltammetry technique (**Figure 2f**). The CO stripping potential of Pd/Py-COF and Pd/Be-COF respectively at 0.84 V and 0.85 V showed the similar electronic structure of the two catalysts. The CO stripping potential of Pd/COFs is higher than that of Pd/C (0.72 V), suggesting the C-O bond weakening by the back-donation of electrons from electronic rich Pd/COFs to the 2π* antibonding orbitals of CO31. The similar electronic and geometric structure for the three catalysts is possibly related to the 2D layered stacking structures of the COFs32 and the strong coordination of N with Pd than the other functional groups in the COFs33.

Promotion effect of p-p interactions in Pd catalysed hydrogenation

On the basis of the above characterizations, Pd NPs in the three COFs with identical size, surface electronic/geometric structure but different chemical environment were used as model catalysts to investigate the effect of the no-covalent interactions on the catalytic performance of metal NPs. Considering the tilting adsorption configuration of aromatic carbonyls on the Pd surface[34] would interact with the conjugation skeleton of COFs, acetophenone (AP) hydrogenation was selected as the model reaction. AP hydrogenation with Pd NPs could produce phenyl ethanol and ethylbenzene under mild conditions (**Figure 3**). At 40 ^{o}C and 10 bar H_2, Pd/Py-COF could efficiently catalyse the hydrogenation of AP with > 99% conversion and > 99% selectivity to phenyl ethanol in 3 h. Further prolonging the reaction time after 100% AP conversion, no conversion of phenyl ethanol to side products could be observed with Pd/Py-COF (**Figures 3a, 3b**). Under identical conditions, Pd/Be-COF and Pd/TB-COF also exhibited high selectivity to phenyl ethanol (> 99%) although the conversion was much lower than that of Pd/Py-COF (**Figures 3a,S5d**, **Table S2**). The apparent TOF calculated with ~10% AP conversion of Pd/Py-COF is almost 5.5 and 6.5-fold that of Pd/Be-COF and Pd/TB-COF, respectively. No direct relation of the BET surface area, Pd particle size and surface structure with the activity of Pd/COFs could be observed. In contrast to Pd/COFs, no phenyl ethanol was detected with Pd/C as the catalyst in 3 h and the main products were ethylbenzene and ethylcyclohexane (**Table S2**), suggesting that the activity and selectivity of AP hydrogenation changed obviously via modulation the microenvironment surrounding the Pd NPs.

To identify the key factors of the microenvironment on the catalytic performance of Pd NPs, H-D exchange experiment was first performed to characterize the H_2 dissociation ability of the supported Pd NPs (**Figure 3c, Table S3**). Pd/Py-COF and Pd/Be-COF have almost the same HD formation rate, lower than that of Pd/C. The high selectivity of Pd/COFs is partly related with the weakened Pd–H which suppresses the further hydrogenolysis of C-O bond of phenyl ethanol[34]. Considering the similar H-D formation rate of Pd/Py-COF and Pd/Be-COF, the different catalytic activity of the two samples is not related with the H_2 dissociation ability.

With Pd/Py-COF and Pd/Be-COF as the model catalysts, the reaction order against H_2 and AP was measured. As shown in **Figure 4a**, Pd/Py-COF and Pd/Be-COF have similar reaction orders with respect to H_2 (+0.14 and +0.13). According to the dual site Langmuir-Hinshelwood mechanism, the approximately

half and first order in H_2 at low H_2 pressure suggests the first hydrogenation and the second hydrogenation is the rate-determining step (RDS), respectively (**Eq. 6-7** in the **Supplementary Methods**). Density functional theory (DFT) calculation demonstrated that the sequential hydrogenation of the O atom followed by the C atom in the carbonyl group has much lower free energy barrier than the opposite sequence (**Figure 4b**, 0.198 eV vs. 0.631 eV), consistent with the kinetic results[35]. Therefore, the RDS for Pd/Py-COF and Pd/Be-COF is the same and involves the O hydrogenation step. The apparent activation energies of AP hydrogenation were respectively 51.1 kJ/mol and 60.2 kJ/mol for Pd/Py-COF and Pd/Be-COF (**Figure 3d**). The above thermodynamic and kinetic studies suggest that Pd/Py-COF and Pd/Be-COF with the same reaction pathways have different activation energy for AP hydrogenation.

DFT calculations were carried out to clarify the different activation barriers of Pd/Py-COF and Pd/Be-COF using a simply model with Pd_4 cluster loaded on Py-COF and Be-COF. As shown in **Figure S7**, the dissociated hydrogen atoms were subsequently transferred to the oxygen atom of C=O group by overcoming barriers of 1.00 eV (transition state, TS) over Pd_4/Py-COF. However, a higher O hydrogenation barrier (1.35 eV) was observed for Pd/Be-COF. The result suggested that the TS stabilized by Pd via the phenyl ring of AP could significantly decrease the energy of O hydrogenation step. This also indirectly suggests that AP hydrogenation on Pd/Py-COF is more favourable than that on Pd/Be-COF, possibly due to stabilization of the TS via π-π interaction between pyrene rings and AP. The orders with respect to AP is respectively ~0 and +0.36 for Pd/Py-COF and Pd/Be-COF, indicating the stronger adsorption of AP on Pd/Py-COF than that on Pd/Be-COF[36]. We infer that the strong interaction results from the direct preferential adsorption of carbonyl group on the Pd surface via the π-π interaction between pyrene rings and AP.

To identify the interaction between AP and COFs, we performed the IR spectra for adsorption tests of AP on the Pd/Py-COF and Pd/Be-COF catalysts (**Figures 4c, S8**). The new IR band of C=O vibration at 1681 cm^{-1} appears for Pd/Py-COF and Pd/Be-COF with adsorbed AP. In comparison with AP, the red shifts of the C=O band from 1686 cm^{-1} to 1681 cm^{-1} indicates the coordination of C=O with surface Pd. In addition to C=O vibration, the band of aromatic C-H of AP at ~1586 cm^{-1} could also be observed for Pd/Py-COF, implying that the stronger interaction between AP and Pd/Py-COF via π-π interaction. This peak was covered by the C=C vibrations of Pd/Be-COF. The calculated interaction energies between AP and Py-COF are much higher than that with Be-COF (12.81 vs. 11.8 kcal mol^{-1}, **Figures 4d, S9**), consistent with the previous reports that pyrene is easy to form π−π interactions with aromatics due to its planar conjugated electronic structure. This is also confirmed by the obvious broadening of the H signals in ^{1}H-NMR spectrum of AP in the presence of pyrene but not in the presence of mesitylene (**Figure S10**).

With an aim to further prove the accelerating effect of π-π interactions in AP hydrogenation, the activity of Pd/Py-COF and Pd/Be-COF was tested in the hydrogenation of cyclohexanone (CHO) which has similar carbonyl group to AP but without the aromatic ring (**Figure 4d**). The calculated interaction energies of CHO with Py-COF and Be-COF are similar (9.06 vs. 9.07 kcal mol^{-1}), signifying the important role of π-π interactions in AP adsorption. Pd/Py-COF and Pd/Be-COF could efficiently catalyse the CHO

hydrogenation to cyclohexanol with > 99% selectivity. Notably, Pd/Py-COF and Pd/Be-COF afforded almost the same TOFs (28 vs. 27 h^{-1}), showing that the two catalysts have similar activity in CHO hydrogenation. This is quite different from the activity sequence in AP hydrogenation. Based on all the experimental and theoretical results, the relative strong p-p interactions of Py-COF and AP reduce the activation barrier in the RDS involving the O hydrogenation step, which promote both the activity and selectivity in AP hydrogenation to phenyl ethanol (**Figure 4e**). The process was then boosted by the rapid desorption of phenyl ethanol considering that the adsorption of C=O on Pd surface is stronger than that of hydroxyl group[37].

Generality of the activity promotion effect of p-p interactions

The generality of the activity promotion effect of p-p interactions was tested in the hydrogenation of a series of aromatic carbonyls with Pd/Py-COF and Pd/Be-COF as model catalysts (**Table 1, Entries 1-3**). In addition to AP, Pd/Py-COF could efficiently catalyze the hydrogenation of 2-acetonaphthone and 2-naphthaldehyde to the corresponding alcohols with > 99% conversion and > 99% selectivity. In comparison with AP, it needs longer reaction time to reach > 99% conversion for 2-acetonaphthone, which is related with more rigid and conjugated structure of 2-acetonaphthone. The activity of Pd/Py-COF is more enhanced for the hydrogenation of 2-acetonaphthone than that for AP (6.1 vs. 5.5-fold as high as that of

Table 1. Comparison of the activity of Pd/Py-COF and Pd/Be-COF in the hydrogenation reactions.[a]

Entry	Substrates	Products	t (h)	Conv. (%)	Sel. (%)	TOF (h^{-1})[b]	Ratio of TOF[c]
1			3	> 99	> 99	275 (50)	5.5
2			10	> 99	> 99	92 (15)	6.1
3			1	> 99	> 99	641 (195)	3.3
4			3	> 99	> 99	277 (50)	5.6
5			2.5	> 99	> 99	389 (134)	2.9
6			0.75	> 99	> 99	15751 (5529)	2.9
7			1	98	99	24015 (6015)	4.0
8			1	52	> 99	439 (38)	11.6

[a]Reaction conditions: 40 ^{o}C, 10 bar of H_2, 2 mL of EtOH, entries 1-5: 0.3 mmol of substrates, Pd catalysts 0.833mol%; entry 6: 8 mmol of substrates, Pd catalysts 0.05 mol%; entry 7: 8 mmol of substrates, Pd catalysts 0.02 mol%. Data in parentheses refer to Pd/Be-COF. [b]TOF was calculated with a conversion less than 30%. [c]The ratio of TOF of Pd/Py-COF and of Pd/Be-COF.

Pd/Be-COF), implying that stronger p-p interactions favor higher activity. As for 2-naphthaldehyde, Pd/Py-COF is 3.3-fold as active as Pd/Be-COF. Interestingly, we also found that Pd/Py-COF is more active than Pd/Be-COF in the hydrogenation of benzofuran to 2, 3-dihydrobenzofuran (5.6-fold), quinoline to 1, 2, 3, 4-tetrahydroquinoline (2.9-fold), N-benzylidenemethylamine to N-benzylmethylamine (2.9-fold) and nitrobenzene to aniline (4.0-fold, **Table 1, Entries 4-7**). For the hydrogenation of furfural to tetrahydrofurfuryl alcohol, the activity of Pd/Py-COF is more than one order that of Pd/Be-COF (439 vs. 38 h^{-1}, **Table 1, Entry 8**). Furthermore, we also tested the activity of Pd/Py-COF and Pd/Be-COF in the hydrogenation of styrene to ethylene benzene. Different from the above substrates, Pd/Py-COF with 8090 h^{-1} TOF is less active than Pd/Be-COF with 12830 h^{-1} TOF, indicating that the π-π interaction does not promote the hydrogenation activity of non-polar groups. This may be related with the different reaction mechanism and adsorption mode of polar and non-polar group on the metal surface[38]. The above results suggest that the π–π interactions could promote the activity of Pd NPs in the hydrogenation of polar functional group of aromatic compounds.

We also tested the recycling stability of Pd/Py-COF with AP hydrogenation as the model reaction (**Figure S11**). After reaction, the catalyst recovered by centrifugation was washed thoroughly with ethanol and dried under vacuum. The recovered catalyst was directly used for the next run. Pd/Py-COF could be stably recycled for 4 cycles without obvious loss of catalytic activity and selectivity. After the fourth cycle, no aggregation of Pd NPs could be observed in the TEM image of used Pd/Py-COF (**Figure S11b**), demonstrating the high recycling stability of Pd/Py-COF.

Conclusion

In summary, Pd/Py-COF showed much higher activity than Pd/Be-COF and Pd/TB-COF in hydrogenation of AP to phenyl ethanol, though the three catalysts have similar Pd size and surface structure. The reaction mechanism investigations and DFT calculations suggest that the activation barriers in the RDS involving the O hydrogenation step is reduced by the p-p interaction among pyrene and AP. In addition to AP hydrogenation, pyrene rings in the skeleton of COFs can greatly improve the activity of Pd NPs in the selective hydrogenation of a series of polar groups (C=O, NO_2, C=N) of aromatic compounds. In contrast, the activity promotion effect of pyrene cannot be observed in the hydrogenation of cyclohexanone to cyclohexanol, confirming the important role of the non-covalent p-p interactions in the activity promotion. The promotion effect of the p-p interactions in the catalytic activity signifies the importance of the weak interactions in modulation the catalytic performance of heterogeneous catalysts beyond the active sites.

Methods

Preparation of Py-DMTA-COF (Py-COF). Specifically, 0.5 mmol of 1, 3, 6, 8-tetrakis (4-aminophenyl) pyrene (Py) and 1 mmol of 2, 5-dimethoxyterephthalaldehyde (DMTA) were dissolved in a mixture of solvents containing 10 mL of o-dichlorobenzene and 5 mL of 1-butanol. 1 mL 6 M CH_3COOH was successively added into the mixture (the solvent screening see **Table S4**). After sonification for 2 min, the

mixture was heated at 85 ^{o}C for 120 h under N_2 atmosphere. The solid product was recovered by filtration and washed with copious amounts of methanol, followed by Soxhlet extraction using THF for 24 h. After drying under vacuum at 60 ^{o}C for 6 h, the orange solid was obtained with a yield of 91%. The material was denoted as Py-COF. The control materials, TPB-DMTA-COF (Be-COF) and BND-TFPB-COF (TB-COF) were prepared according to the literature reports[27,28].

Preparation of Pd/Py-COF. Typically, Pd/Py-COF with 5 wt% Pd loading was prepared by a traditional impregnation-reduction method. 95 mg of Py-COF was dispersed in 4 mL of deionized water, followed by the addition of 0.5 mL of Na_2PdCl_4 aqueous solution (0.01 g mL^{-1}). After stirring for 3 h, the solid was separated by filtration and washed with water. After drying at 100 ^{o}C for 30 min, the orange red powder was reduced at 200 ^{o}C in H_2 for 2 h (2 ^{o}C/min). The preparation method of Pd/Be-COF and Pd/TB-COF was similar with Pd/Py-COF except that the Be-COF/TB-COF was used.

Catalyst Characterizations. N_2 sorption isotherms were performed on a Micromeritics ASAP 2020 system volumetric adsorption analyser. FT-IR spectra in the range of 400 to 4000 cm^{-1} were collected with a Nicolet Nexus 470 IR spectrometer using KBr pellets. Solid-state ^{13}C CP TOSS (total suppression of spinning sidebands) spectra were recorded on a Bruker 600 MHz spectrometer. Transmission electron microscopy (TEM) was performed using a HITACHI HT7700 at an accelerating voltage of 100 kV. High-resolution scanning electron microscopy (HRSEM) was undertaken by using a HITACHI S5500 apparatus operating at an acceleration voltage of 1–30 kV. The EDS mappings were obtained using a JEOL F200 instrument. Powder Xray diffraction (PXRD) patterns of the samples were measured on a Rigaku RINT D/Max-2500 powder diffraction system operated at 40 kV and 200 mA using Cu Kα radiation (a scan rate of 5^{o} min^{-1}). X-ray photoelectron spectroscopy (XPS) was recorded on a VG ESCALAB MK2 apparatus using Al K_α (h_λ = 1486.6 eV) as the excitation light source. The metal contents of the samples were determined using a PLASAM- SPEC-II inductively coupled plasma atomic emission spectrometer (ICP) by digesting the COFs in HNO_3/H_2SO_4 (1: 1, v/v).

In situ FT-IR of CO adsorption. The in situ FT-IR of CO adsorption spectra were collected on a Bruker EQUINOX 55 infrared spectrometer with a MCT detector. Before the measurement, the catalyst was pre-treated at 200 °C under a flowing H_2 atmosphere (20 mL min^{-1}) for 1 h. The catalyst was subsequently cooled to room temperature. After the system was purged with Ar for 30 min, the background spectrum was collected. CO adsorption experiments were carried out by collecting 64 scans at a resolution of 4 cm^{-1}. Gas-phase CO spectra were collected at the same pressure and subtracted from the corresponding sample spectra.

CO chemisorption experiments. CO chemisorption measurement was performed at 50 °C on Autochem II 2920 chemisorption instrument with a thermal conductivity detector (TCD). For CO chemisorption, the sample (~100 mg) was pre-treated with hydrogen at desired temperatures for 1 h, followed by purging with high-purity He for 30 min. After cooling down to 50 °C, a 5% CO mixture was injected into the reactor

repeatedly until CO adsorption was saturated. The dispersion of Pd was calculated from the adsorbed amount of CO by assuming the CO/Pd adsorption stoichiometry to be 1/2[31].

H–D exchange. H–D exchange experiments were carried out in a flow quartz reactor at 22 °C[39]. The formation rate of HD was measured by mass signal intensity (ion current). Before the test, the catalysts were heated in H_2 (10 mL min^{-1}) at 200 °C for 20 min. After cooling to room temperature, D_2 (10 mL min^{-1}) mixed with H_2 was passed through the sample. The gas hourly space velocity (GHSV) is 4.64 × 10^7 mL h^{-1} g_{metal}^{-1}. Under these conditions, the H–D exchange conversion were always kept below 15% for calculation of turnover frequency (TOF). Products (HD, H_2, and D_2) were analysed with an online mass spectrometer (GAM200, InProcess Instruments). The mass/charge ratio (m/z) values used are 2 for H_2, 4 for D_2, and 3 for HD. The background HD exchanges from the corresponding support were deducted from the results.

Catalytic hydrogenations. The hydrogenation reactions were carried out in a stainless-steel autoclave (300 mL) with a thermocouple-probed detector. Typically, a desired amount of the solid catalyst (2.5 × 10^{-3} mmol Pd) was placed in an ampule tube, followed by the addition of AP (0.3 mmol) (S/C = 120) and 2 mL solvent. The ampule tube was loaded into the reactor. After the tube was purged six times with hydrogen, the final pressure was adjusted to 10 bar and the reactor was heated to 40 ^{o}C with vigorous stirring. To ensure the collection of reliable catalytic data, the experiments were carried out at different stirring rates and the results showed that the reaction rate remained constant in the range of 800–1000 rpm, suggesting no influence of the external diffusion. The solvent was also optimized and the results show that EtOH is the best solvent for AP hydrogenation among the investigated protic and aprotic solvent (**Table S5**). After the reaction, the solid catalyst was separated by centrifugation and the filtrate was collected, diluted with EtOH and analyzed by an Agilent 7890B GC equipped with an Agilent J&W GC HP-5 capillary column (30 m × 0.32 mm × 0.25 μm). In the recycle test, the catalyst recovered by centrifugation was washed with EtOH and used in the next run directly.

Declarations

Associated content

The Supporting Information is available free of charge on the xxx…

Author information

Corresponding Authors

*E-mail: yangqh@dicp.ac.cn,

mengfeiluo@zjnu.cn.

ORCID Qihua Yang: 0000-0002-1118-3397

Notes

The authors declare no competing interests.

Acknowledgments

We acknowledge financial support from the National Key R&D Program of China (2017YFB0702800), the National Natural Science Foundation of China (21733009), and the Strategic Priority Research Program of the Chinese Academy of Sciences (XDB17020200).

Author contributions

M. G. was responsible for most of the investigations, methodology development, data collection and analysis, and writing the original manuscript. S. J. designed and synthesized the Py-COF materials. X. T. K. carried out the part of the density functional calculations. C. Z. L. and H. L. synthesized the Be-COF and TB-COF. Q. H. Y. was responsible for the conceptualization, funding and revising the manuscript.

References

1. Fu, Q. & Bao, X. Confined microenvironment for catalysis control. *Nat. Catal.* **2**, 834-836 (2019).

2. Jiao, L., Wang, J. & Jiang, H. L. Microenvironment modulation in metal–organic framework-based catalysis. *Acc. Mater. Res.* **2**, 327-339 (2021).

3. Li, H., Xiao, J., Fu, Q. & Bao, X. Confined catalysis under two-dimensional materials. *Proc. Natl Acad. Sci. USA* **114**, 5930–5934 (2017).

4. Schwartz, T. J., Johnson, R. L., Cardenas, J., Okerlund, A., Da Silva, N. A., Schmidt-Rohr, K. & Dumesic, J. A. Engineering catalyst microenvironments for metal-catalyzed hydrogenation of biologically derived platform chemicals. *Angew. Chem.* **126**, 12932-12936 (2014).

5. Thomas, J. M. & Williams, R. J. Philos. Catalysis: principles, progress, prospects. *Philos. Trans. R. Soc. A. Math. Phys. Eng. Sci.* **363**, 765–791 (2005).

6. Catlow, C. R. A., French, S. A., Sokol, A. A. & Thomas, J. M. Computational approaches to the determination of active site structures and reaction mechanisms in heterogeneous catalysts. *Philos. Trans. R. Soc. A. Math. Phys. Eng. Sci.* **363**, 913-936 (2005).

7. Schoenbaum, C. A., Schwartz, D. K. & Medlin, J. W. Controlling the surface environment of heterogeneous catalysts using self-assembled monolayers. *Acc. Chem. Res.* **47**, 1438-1445 (2014).

8. Liu, K., Qin, R. & Zheng, N. Insights into the interfacial effects in heterogeneous metal nanocatalysts toward selective hydrogenation. *J. Am. Chem. Soc.* **143**, 4483-4499 (2021).

9. Yan, J., Teo, B. K. & Zheng, N. Surface chemistry of atomically precise coinage–metal nanoclusters: from structural control to surface reactivity and catalysis. *Acc. Chem. Res.* **51**, 3084-3093 (2018).

10. Koy, M., Bellotti, P., Das, M. & Glorius, F. N-Heterocyclic carbenes as tunable ligands for catalytic metal surfaces. *Nat. Catal.* **1-12** (2021).

11. Kahsar, K. R., Schwartz, D. K. & Medlin, J.W. Control of metal catalyst selectivity through specific noncovalent molecular interactions. *J. Am. Chem. Soc.* **136**, .520-526 (2014);

12. Pang, S. H., Schoenbaum, C. A., Schwartz, D. K. & Medlin, J. W. Directing reaction pathways by catalyst active-site selection using self-assembled monolayers. *Nat. Commun.* **4**, 1-6 (2013).

13. Marshall, S. T., O'Brien, M., Oetter, B., Corpuz, A., Richards, R. M., Schwartz, D. K. & Medlin, J. W. Controlled selectivity for palladium catalysts using self-assembled monolayers. *Nat. Mater.* **9**, 853–858 (2010).

14. Zhao, X. J., Zhou, L. Y., Zhang, W. Y., Hu, C. Y., Dai, L., Ren, L. T., Wu, B. H., Fu, G. & Zheng, N. F. Thiol treatment creates selective palladium catalysts for semihydrogenation of internal alkynes. *Chem*, **4**, 1080–1091 (2018).

15. Lee, S. Y., Shin, S. J., Baek, H. Y., Choi, Y. W., Hyun, K. L., Seo, M., Kim, K., Koh, D. Y., Kim, H. J. & Choi, M. Dynamic metalpolymer interaction for the design of chemoselective and long-lived hydrogenation catalysts. *Sci. Adv.* **6**, No. eabb7369 (2020).

16. Burgi, T. & Baiker, A. Heterogeneous enantioselective hydrogenation over cinchona alkaloid modified platinum: mechanistic insights into a complex reaction. *Acc. Chem. Res.* **37**, 909–917 (2004).

17. Schwalm, O., Minder, B., Weber, J. & Baiker, A. Enantioselective hydrogenation of alpha-ketoesters over Pt/alumina modified with cinchonidine-theoretical investigation of the substrate-modifier interaction. *Catal. Lett.* 23, 271–279 (1994).

18. Zhao, M., Yuan, K., Wang, Y., Li, G., Guo, J., Gu, L., Hu, W., Zhao, H. & Tang, Z. Metal-organic frameworks as selectivity regulators for hydrogenation reactions. *Nature* **539**, 76-80 (2016).

19. Ren, X., Guo, M., Li, H., Li, C., Yu, L., Liu, J. & Yang, Q. Microenvironment engineering of ruthenium nanoparticles incorporated into silica nanoreactors for enhanced hydrogenations. *Angew. Chem. Int. Ed.* **58**, 14483-14488 (2019).

20. Riscoe, A. R., Wrasman, C. J., Herzing, A. A., Hoffman, A. S., Menon, A., Boubnov, A., Vargas, M., Bare, S. R. & Cargnello, M. Transition state and product diffusion control by polymer-nanocrystal hybrid catalysts. *Nat. Catal.* **2**, 852-863 (2019).

21. Geng, K., He, T., Liu, R., Dalapati, S., Tan, K. T., Li, Z., Tao, S., Gong, Y., Jiang, Q. & Jiang, D. Covalent organic frameworks: design, synthesis, and functions. *Chem. Rev.* **120**, 8814-8933 (2020).

22. Colson, J. W. & Dichtel, W.R. Rationally synthesized two-dimensional polymers. *Nat. Chem.* **5**, 453-465 (2013).

23. Jin, Y., Hu, Y. & Zhang, W., Tessellated multiporous two-dimensional covalent organic frameworks. *Nat. Rev. Chem.* **1**, 1-11 (2017).

24. Diercks, C. S. & Yaghi, O. M. The atom, the molecule, and the covalent organic framework. *Science* **355**, No. 6328, (2017).

25. Wu, Y., Xu, H., Chen, X., Gao, J. & Jiang, D. A π-electronic covalent organic framework catalyst: π-walls as catalytic beds for Diels–Alder reactions under ambient conditions. *Chem. Commun.* **51**, 10096-10098 (2015).

26. Yang, Y., Deng, D., Zhang, S., Meng, Q., Li, Z., Wang, Z., Sha, H., Faller, R., Bian, Z., Zhou, X., Zhu, G. & Yuan, Y. Porous organic frameworks featured by distinct confining fields for the selective hydrogenation of biomass-derived ketones. *Adv. Mater.* **32**, 1908243 (2020).

27. Xu, H., Gao, J. & Jiang, D. Stable, crystalline, porous, covalent organic frameworks as a platform for chiral organocatalysts. *Nat. Chem.* **7**, 905-912 (2015).

28. Li, C., Ren, X., Guo, M., Li, W., Li, H., & Yang, Q. Highly active ultrafine Pd NPs confined in imine-linked COFs for nitrobenzene hydrogenation. *Catal. Sci. Technol.* **11**, 3873-3879 (2021).

29. Georgakilas, V., Tiwari, J. N., Kemp, K. C., Perman, J. A., Bourlinos, A. B., Kim, K. S. & Zboril, R. Noncovalent functionalization of graphene and graphene oxide for energy materials, biosensing, catalytic, and biomedical applications. *Chem. Rev.* **116**, 5464-5519 (2016).

30. Ding, S. Y., Gao, J., Wang, Q., Zhang, Y., Song, W. G., Su, C. Y. & Wang, W. Construction of covalent organic framework for catalysis: Pd/COF-LZU1 in Suzuki-Miyaura coupling reaction. *J. Am. Chem. Soc.* **133**., 19816-19822 (2011).

31. Guo, M., Li, C. & Yang, Q. Accelerated catalytic activity of Pd NPs supported on amine-rich silica hollow nanospheres for quinoline hydrogenation. *Catal. Sci. Technol.* **7**, 2221-2227 (2017).

32. Spitler, E. L., Koo, B. T., Novotney, J. L., Colson, J. W., Uribe-Romo, F. J., Gutierrez, G. D., Clancy, P. & Dichtel, W. R. A 2D covalent organic framework with 4.7-nm pores and insight into its interlayer stacking. *J. Am. Chem. Soc.* **133**, 19416-19421 (2011).

33. Kuo, C. T., Lu, Y., Arab, P., Weeraratne, K. S., El-Kaderi, H., & Karim, A. M. 18.1% single palladium atom catalysts on mesoporous covalent organic framework for gas phase hydrogenation of ethylene. *Cell Rep. Phys. Sci.* **2**, 100495 (2021).

34. Guo, M., Li, H., Ren, Y., Ren, X., Yang, Q. & Li, C. Improving catalytic hydrogenation performance of Pd nanoparticles by electronic modulation using phosphine ligands. *ACS Catal.* **8**, 6476-6485 (2018).

35. Zhao, Z., Bababrik, R., Xue, W., Li, Y., Briggs, N. M., Nguyen, D. T., Nguyen, U., Crossley, S. P., Wang, S., Wang, B. & Resasco, D. E. Solvent-mediated charge separation drives alternative hydrogenation path of furanics in liquid water. *Nat. Catal.* **2**, 431-436 (2019).

36. Guo, M., Kong, X., Li, C., & Yang, Q. Hydrogenation of benzoic acid derivatives over Pt/TiO_2 under mild conditions. *Commun. Chem.* **4**, 1-10 (2021).

37. Chen, M., Maeda, N., Baiker, A. & Huang, J. Hydrogenation of acetophenone on Pd/silica–alumina catalysts with tunable acidity: mechanistic insight by in situ ATR-IR spectroscopy. *ACS Catal.* **8**, 6594-6600 (2018).

38. Zaera, F. Key unanswered questions about the mechanism of olefin hydrogenation catalysis by transition-metal surfaces: a surface-science perspective. *Phys. Chem. Chem. Phys.* **15**, 11988-12003 (2018).

39. Guo, M., Peng, J., Yang, Q. & Li, C. Highly active and selective RuPd bimetallic NPs for the cleavage of the diphenyl ether C–O bond. *ACS Catal.* **8**, 11174-11183 (2018).

Figures

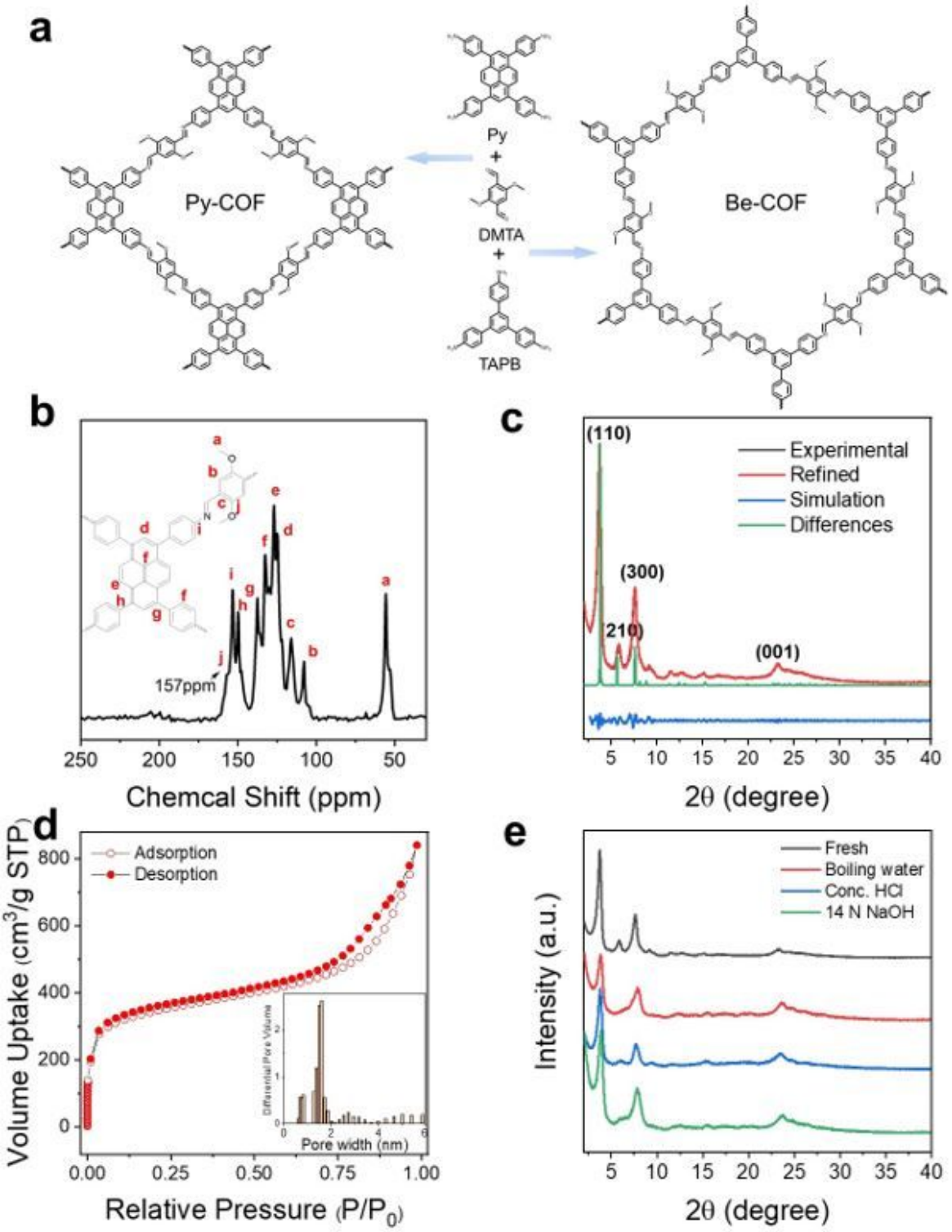

Figure 1

Synthesis, characterizations and stability test of COFs. a Synthesis of Py-COF and Be-COF by condensation of DMTA with Py and TAPB, respectively. b 13C CP-TOSS NMR spectrum, c Experimental, Pawley-refined and simulated PXRD patterns (AA stacking) and difference plot, d N2 adsorption isotherm and pore size distribution and e PXRD patterns of Py-COF before and after treatment in boiling water, 12N HCl and 14N NaOH for 3 days.

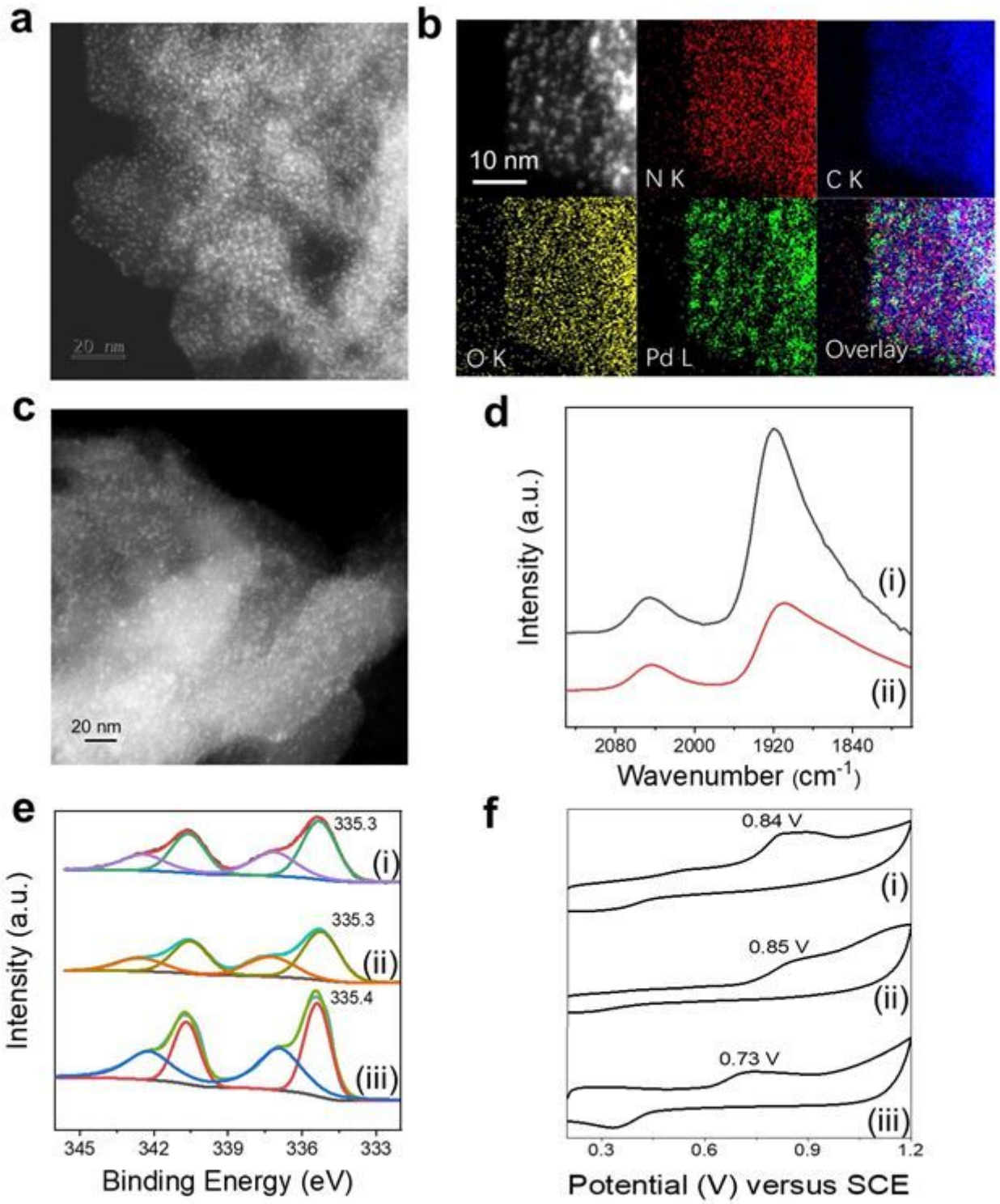

Figure 2

Characterization of supported Pd NPs. a HAADF-STEM image and b N, C, O, and Pd STEM-EDS maps and reconstructed overlay image for Pd/Py-COF. c HAADF STEM image of Pd/Be-COF. d In situ FTIR spectra of CO adsorption, e Pd 3d XPS core level spectra and f CO stripping voltammetry of (i) Pd/Py-COF, (ii) Pd/Be-COF and (iii) Pd/C.

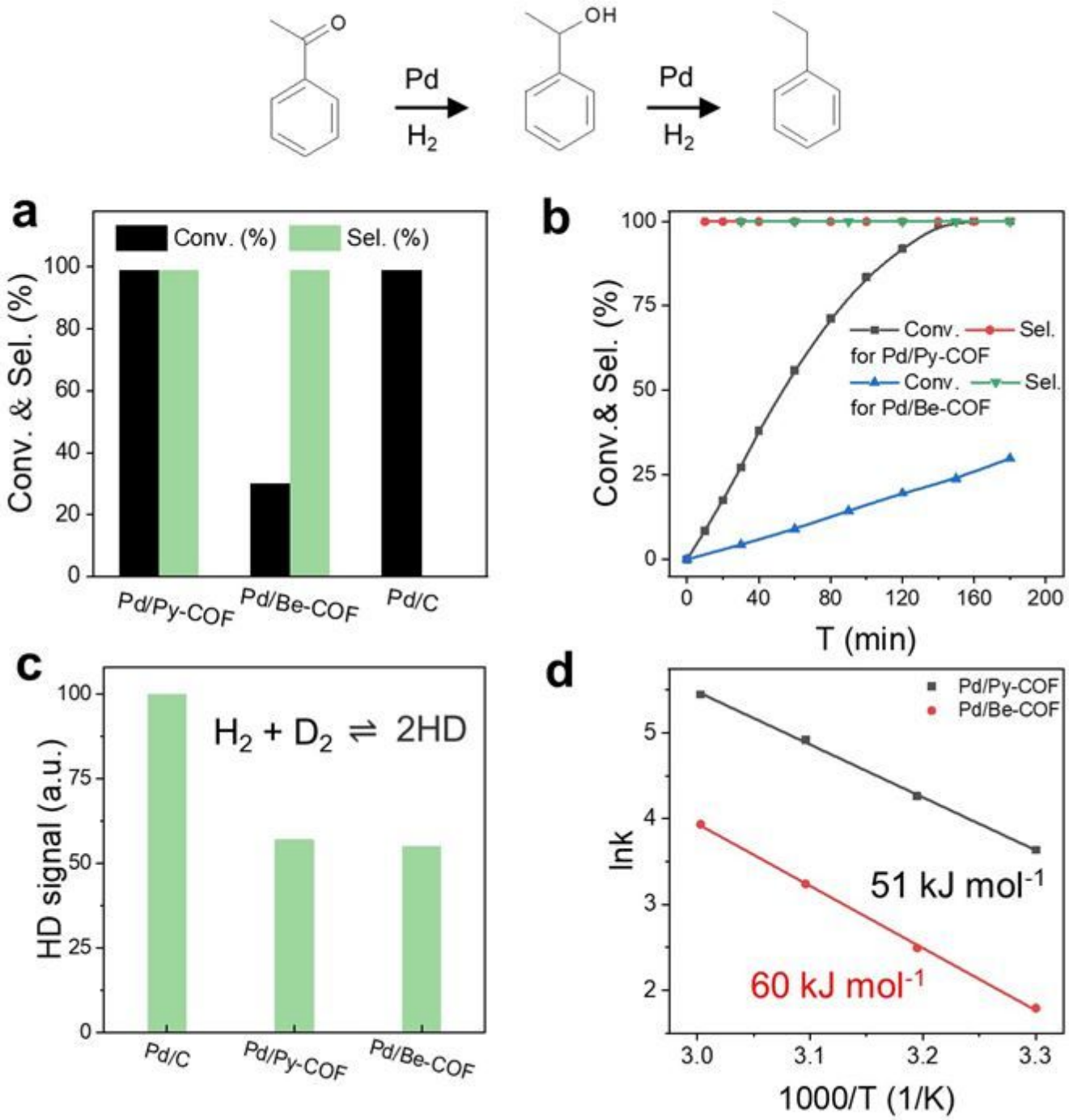

Figure 3

AP hydrogenation on supported Pd NPs. a The comparison of the conversion and phenyl ethanol selectivity and b reaction profiles of supported Pd NPs in AP hydrogenation. c H-D exchange results of supported Pd NPs. d Arrhenius plots showing apparent activation barriers for (i) Pd/Py-COF and (ii) Pd/Be-COF.

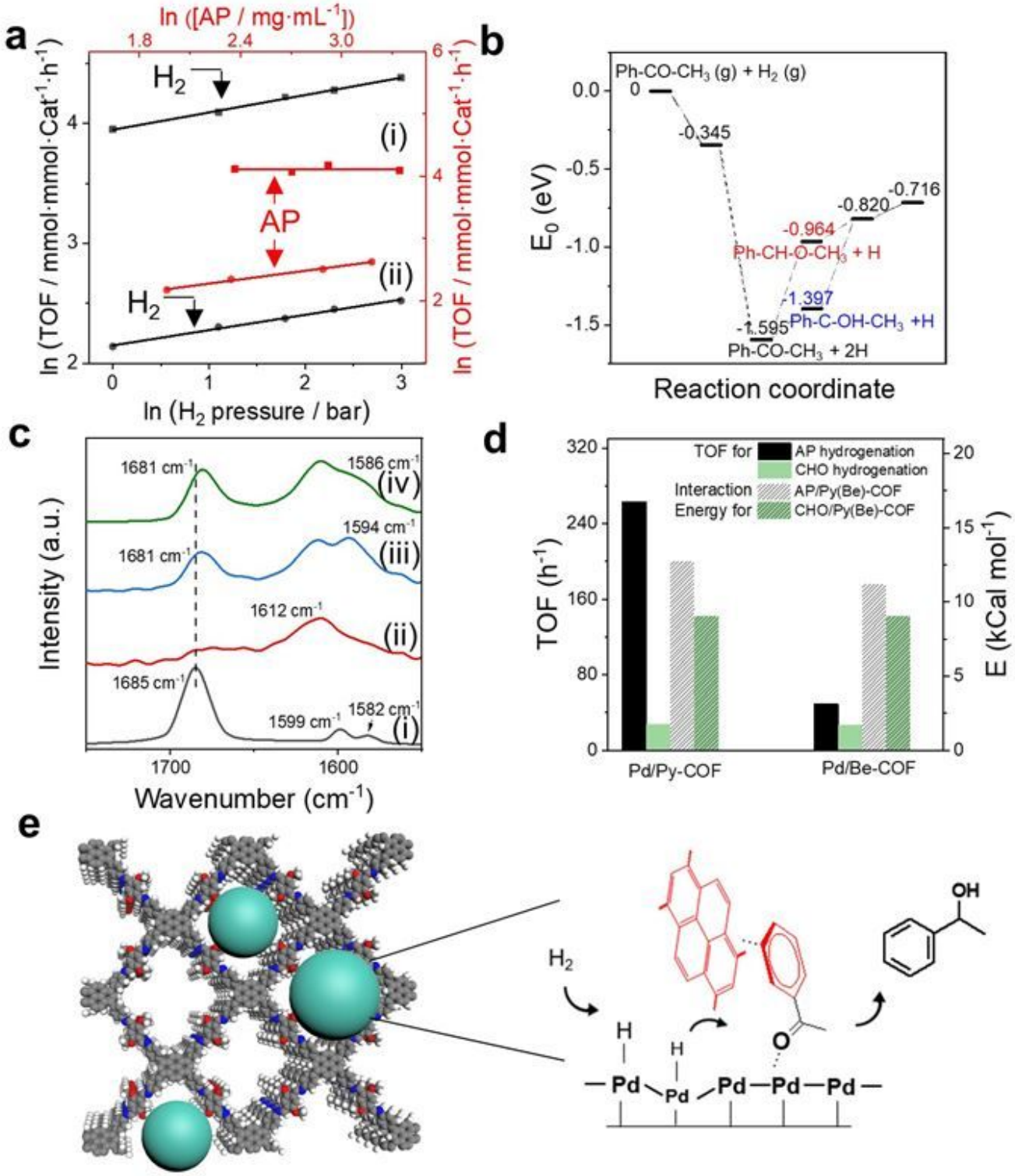

Figure 4

Mechanism investigation. a Reaction orders against H2 and AP for (i) Pd/Py-COF and (ii) Pd/Be-COF. b Potential energy profiles for carbonyl hydrogenation of AP with different sequences (O1stC2nd and C1stO2nd). c FT-IR spectra of (i) AP, (ii) Pd/Py-COF and AP absorbed on (iii) Pd/Py-COF and (iv) Pd/Be-COF. d TOFs of AP and CHO hydrogenation on Pd/Py-COF and Pd/Be-COF and the interaction energies

between COFs and AP/CHO. e Schematic diagram of Pd NPs confined in Py-COF and proposed reaction mechanism of AP hydrogenation on Pd/Py-COF.

Supplementary Files

This is a list of supplementary files associated with this preprint. Click to download.

- SI.docx